JAXA Research and Development Report

MID-INFRARED VARIABILITY OF ACTIVE GALACTIC NUCLEI WITH THE *AKARI* AND *WISE* ALL-SKY SURVEYS

K. MATSUTA, T. DOTANI, P. GANDHI, T. NAKAGAWA,
K. ENYA, H. MATSUHARA, S. TAKITA and Y. TOBA

February 2017

Japan Aerospace Exploration Agency

MID-INFRARED VARIABILITY OF ACTIVE GALACTIC NUCLEI WITH THE *AKARI* AND *WISE* ALL-SKY SURVEYS

K. Matsuta[1, 2, 4], T. Dotani[1, 2], P. Gandhi[2, 3], T. Nakagawa[2], K. Enya[1, 2], H. Matsuhara[1, 2], S. Takita[2], Y. Toba[1, 2]

ABSTRACT

We studied mid-infrared (mid-IR) variability of AGN systematically combining two all-sky survey catalogs released by *AKARI* and Wide-field Infrared Survey Explorer (*WISE*). Because the two surveys are separated by ∼4 years, our studies are sensitive to variations of time scales of a few years. We started with the list of AGN selected by Matsuta et al. (2012) from the cross-identification of *Swift*/BAT and *AKARI* catalogs. The list was further correlated with the *WISE* catalog to select a total of 71 AGN, which were used for the present studies. We compared source fluxes in the *AKARI* S9W (9 μm) and *WISE* W3 (12 μm) bands and in the *AKARI* L18W (18μm) and *WISE* W4 (22 μm) bands carefully correcting for the band differences and considering the systematic effects. We detected significant flux changes from 3 sources, two blazars (3C 273, 3C 345) and a radio galaxy (3C 445), in the mid-IR bands. This is the first detection of mid-IR variability from 3C 445, which may be originated from the jets. We also analyzed average sample variability for different AGN types excluding these 3 variable sources. We detected significant variations from Seyfert 1 in the S9W-W3 band with 95% confidence limit; the average fractional variability reached 13% (6–18%). Two origins are conceivable for the variability: the dusty torus and the jets. If such variability originates from the torus, the dust distribution in the torus should be very narrow, and its radial extent may be much smaller than the distance to the AGN. Alternatively, the variability may result from the jets considered to be present in Seyfert 1 galaxies.

Key words: active galactic nuclei, infrared sources, X-ray sources

1. INTRODUCTION

Active galactic nuclei (AGN) produce enormous amount of energy from the central compact region harboring a super massive black hole. Mass accretion on to the black holes sustain the large luminosity of AGN, although the geometry and emission mechanism in the nuclear region are not well understood yet. Luminosity variations of AGN, which are their common properties, convey precious information to probe the nuclear region unless otherwise difficult to obtain (e.g. Ulrich et al. 1997).

Time variations may have different properties in different wave bands depending on the emission mechanisms. The UV/optical continuum variability tends to be correlated with that of X-rays with little time delay. This means that the UV/optical emission may be due to the reprocessing of the X-ray emission from the central source. Some models explain that the UV/optical emission is produced by an optically thick medium (i.e., accretion disk) irradiated by the variable central X-ray source (Haardt & Maraschi 1993). Infrared (IR) variations have smaller amplitude and longer time scale than those in UV/optical bands (Neugebauer et al. 1989; Hunt et al. 1994). In near-IR band, variations with time scales on the order of years are seen in the radio-loud quasars, whose amplitude is less than 1 mag. Variations of Seyfert 1s and quasars of 226 samples were studied in near-IR for a time scale of a few years (Enya et al. 2002a,b,c). They argued that near-IR variability of the radio-quiet AGN is consistent with a simple dust reverberation, but that of radio-loud AGN may require a non-thermal variable component. On the other hand, in the mid-IR band, there is no strong and rapid variation than that of X-ray and UV/optical emissions except for blazars. A few sources show variability on timescale of a year, whose average amplitude reaches ∼10% at 10 μm with a significant time delay compared to variations of UV/optical continuum (e.g., Clavel et al. 1989; Neugebauer & Matthews 1999; Gorjian et al. 2004; Kozłowski et al. 2010).

Among the time variations in various wave bands, mid-IR variations can potentially constrain the geometry of the dusty torus, because they enable us to measure the response of the torus to changes of the direct emission from the nucleus (Hönig & Kishimoto 2011). However, past observations of mid-IR variability of AGN were made mostly from ground, and were much fewer than those in other wave bands. The situation has changed recently when the all-sky survey data from space became available including the mid-IR band. Therefore, we studied a long-term variation at mid-IR bands by combining the two all-sky survey catalogs, the *AKARI* Point Source Catalogues (*AKARI*/PSC; Ishihara et al. 2010; Yamamura et al. 2010) and the *WISE* All-Sky Source Catalog (*WISE*; Wright et al. 2010). *AKARI* (Murakami et al. 2007) scanned the whole sky twice or more during the 16 months of the cryogenic mission phase in

2006–2007. On the other hand, *WISE* conducted all-sky surveys with high sensitivity in several mid-IR bands in 2010 about 4 years after *AKARI*. As we are interested in variability of AGN, we need to pick up only the AGN from the catalogs. For this purpose, we utilize the cross-identified sources in Matsuta et al. (2012) between the 22-month hard X-ray catalog of *Swift*/BAT (Tueller et al. 2010) and the *AKARI* Point Source Catalogs. The sources were already classified into AGN types, which was very useful for the current studies especially to reveal the AGN type dependence of variability.

This paper is organized as follows. In section 2, we present details of the sample selection and catalog cross-matching. In section 3, we explain the analysis method of variability in the mid-IR band with *AKARI* and *WISE* all-sky surveys. We try to remove the systematic errors as much as possible to evaluate variability of sample AGN. In section 4, we discuss the nature and geometry of AGN inferred from the variability studies. Conclusions are described in section 5. A flat Universe with a Hubble constant $H_0 = 71$ km s^{-1} Mpc^{-1}, $\Omega_\Lambda = 0.73$ and $\Omega_M = 0.27$ is assumed throughout this paper.

2. DATA SELECTION

2.1. *Cross-identification of sources*

We started source selection with the cross-identified sources between *AKARI* and *Swift*/BAT all-sky surveys in Matsuta et al. (2012). Details of the cross-identification are found in Matsuta et al. (2012). In total, 111 and 129 sources were cross-identified between *Swift*/BAT and *AKARI*/IPC 9 and 18 μm band, respectively. These sources are matched with those of the *WISE* All-Sky Source Catalog released in 2012[1].

WISE started all-sky survey from January 7, 2010 with full 4-band (W1, W2, W3, and W4 centered at 3.4, 4.6, 12, and 22 μm, respectively), and the cryogenic survey operations continued until August 6, 2010. We do not use the 3-Band Cryo data acquired after the exhaustion of solid hydrogen because of unavailability of W4 and sensitivity reduction in W3. The *WISE* catalog contains various information on the sources. Among them, the variability flag, *var_flg*, is related to the probability for each band that the source flux is not constant with time (Hoffman et al. 2012). We did not use this flag for the current study of the time variability because the flag only suggest possibility of variations and may not be suited to the quantitative evaluation.

The primary photometric data of *WISE* catalog is based on profile-fit photometry. Although data of aperture photometry are also available, we used profile-fit photometry data because they are relatively insensitive to the source crowding and saturation[2]. The photometric data of *WISE* are given in Vega magnitude computed with the isophotal fluxes in units of Jy, as follows:

$$m = -2.5 \times \log_{10} S_\nu / F_\nu(\text{iso}), \tag{1}$$

where m is Vega magnitude, S_ν is observed fluxes in units of Jy, and $F_\nu(\text{iso})$ is isophotal fluxes. The isophotal fluxes are constant, and are $F_\nu(\text{iso}) = 31.674$ and 8.363 Jy in 12 and 22 μm, respectively (Jarrett et al. 2011). We convert the Vega magnitudes in the *WISE* catalog to Jy in order to compare them with *AKARI* fluxes in Section 3.

When we match the *WISE* catalog with the *Swift*/BAT-*AKARI*/IPC cross-identified sample, we focus on the pairs of the nearest wave bands. This means that the sources cross-identified between *AKARI*/IPC 9 μm and *Swift*/BAT are matched with W3 (12 μm) data in *WISE* catalog. Similarly, those identified between *AKARI*/IPC 18 μm and *Swift*/BAT are matched with W4 (22 μm) data in the *WISE* catalog. We adopt following criteria for cross-matching. Some of them are based on the filters used to generate the *var_flg* flag (Hoffman et al. 2012).

1. Search radius
   We adopted a search radius of $2''$, which is comparable to position accuracy of *WISE* at 3σ level, centered at the position of the optical counterpart listed in the BAT catalog.

2. Signal-to-noise ratio
   We selected only the sources with a photometric quality flag of *ph_qual = A*, indicating a signal-to-noise ratio > 10.

3. Reduced chi-square
   We selected only the sources with chi-square < 5.0 in order to minimize the source confusion.

4. Number of PSF components
   We limited the number of PSF used simultaneously to fit the source image < 3 in order to minimize spurious fluxes by confusion.

5. Active deblending flag
   This flag indicates that a single detection was split into multiple sources in the process of profile-fitting. We selected only the sources which were not actively deblended.

6. Contamination and confusion flag
   This flag, *cc_flg*, indicates contamination or confusion by an image artifact. We selected only the sources unaffected by known artifacts, i.e., *cc_flg=0*.

---

[1] http://irsa.ipac.caltech.edu/Missions/wise.html
[2] http://wise2.ipac.caltech.edu/docs/release/allsky/expsup/sec6_3c.html

7. Saturation

We eliminated bright sources exceeding the saturation level (0.7 and 10 Jy for W3 and W4, respectively). We also excluded sources with high fraction of saturated pixels (i.e., $w1\text{-}4sat \neq 0$).

As a result, among 111/129 AGN of the *Swift*/BAT-*AKARI* (9/18 μm bands) sample, 75 and 109 AGN are detected in W3 (68%) and W4 (84%) bands, respectively. Those not detected in *WISE* are mostly rejected with the criterion of "Reduced chi-square". In what follows, we use only the sources detected in all 4 bands (*AKARI*/IRC 9 and 18 μm bands and *WISE* W3 and W4 bands). This leaves a total of 71 sources. As explained in Section 3.2, the 4-band data are essential to correct band difference between *AKARI* and *WISE*. We summarize parameters of the selected sources (name, IR fluxes, AGN type) inTable 1. Additionally, we list a number of sources for each AGN type in Table 2.

TABLE 1
LIST OF AGN FOR THE CURRENT STUDIES AND THEIR MID-IR FLUXES IN THE *AKARI* AND *WISE* CATALOG

Serial NO. (1)	BAT No. (2)	Object name (3)	F_{S9W} (mJy) (4)	F_{L18W} (mJy) (5)	F_{W3} (mJy) (6)	F_{W4} (mJy) (7)	$\alpha \pm \delta\alpha$ (8)	Type (9)
1	1	Mrk 335	128 ± 3	223 ± 46	163 ± 1	310 ± 3	0.98 ± 0.04	Sy1.2
2	21	NGC 526A	141 ± 14	292 ± 26	140 ± 1	308 ± 3	1.21 ± 0.04	Sy1.5
3	22	Fairall 9	229 ± 20	440 ± 24	262 ± 2	468 ± 4	0.90 ± 0.04	Sy1
4	34	NGC 931	349 ± 12	763 ± 48	427 ± 3	977 ± 9	1.25 ± 0.04	Sy1.5
5	35	IC 1816	55 ± 32	265 ± 20	114 ± 1	369 ± 4	1.81 ± 0.05	Sy1.8
6	37	NGC 985	165 ± 14	368 ± 38	176 ± 1	491 ± 5	1.57 ± 0.04	Sy1
7	41	NGC 1052	146 ± 34	377 ± 17	157 ± 1	445 ± 5	1.61 ± 0.05	Sy2/RL
8	43	[HB89] 0241+622	300 ± 14	635 ± 34	365 ± 3	715 ± 6	1.03 ± 0.04	Sy1/RL
9	50	NGC 1194	169 ± 7	415 ± 56	217 ± 1	524 ± 5	1.35 ± 0.04	Sy1
10	54	NGC 1275	442 ± 26	1988 ± 21	751 ± 5	2900 ± 20	2.08 ± 0.03	Sy2/RL
11	72	IRAS 04124-0803	168 ± 12	423 ± 39	213 ± 1	483 ± 5	1.26 ± 0.04	Sy1
12	77	3C 120	203 ± 20	497 ± 68	232 ± 2	590 ± 5	1.43 ± 0.04	Sy1/RL
13	83	CGCG 420-015	173 ± 7	471 ± 22	253 ± 2	566 ± 5	1.25 ± 0.04	Sy2
14	84	ESO 033-G 002	163 ± 7	387 ± 15	188 ± 1	408 ± 4	1.19 ± 0.04	Sy2
15	85	LEDA 097068	218 ± 13	581 ± 27	277 ± 2	788 ± 7	1.61 ± 0.04	Sy1
16	89	Ark 120	252 ± 18	253 ± 33	227 ± 2	339 ± 4	0.61 ± 0.04	Sy1
17	90	ESO 362-18	166 ± 31	366 ± 36	171 ± 1	478 ± 5	1.58 ± 0.04	Sy1.5
18	93	PKS 0521-36	97 ± 0.1	216 ± 20	115 ± 1	245 ± 2	0.94 ± 0.02	Blazar/BL Lac
19	109	NGC 2110	300 ± 19	566 ± 30	371 ± 3	800 ± 6	1.18 ± 0.04	Sy2
20	112	2MASX J05580206-3820043	348 ± 15	536 ± 17	374 ± 3	575 ± 5	0.66 ± 0.04	Sy1
21	125	Mrk 79	276 ± 6	611 ± 38	297 ± 2	737 ± 8	1.29 ± 0.04	Sy1.2
22	133	Phoenix Galaxy	274 ± 19	1310 ± 6	446 ± 3	1772 ± 15	2.20 ± 0.04	Sy2
23	138	FAIRALL 1146	157 ± 14	441 ± 30	196 ± 1	535 ± 5	1.54 ± 0.04	Sy1.5
24	146	Mrk 704	256 ± 30	469 ± 20	284 ± 2	510 ± 6	0.91 ± 0.05	Sy1.5
25	149	MCG +04-22-042	78 ± 15	178 ± 47	104 ± 1	210 ± 2	1.08 ± 0.05	Sy1.2
26	152	Mrk 705	99 ± 21	214 ± 44	109 ± 1	254 ± 3	1.31 ± 0.05	Sy1.2
27	154	MCG -05-23-016	384 ± 14	1391 ± 21	633 ± 4	1843 ± 9	1.65 ± 0.03	Sy2
28	164	NGC 3227	444 ± 71	1128 ± 44	513 ± 4	1516 ± 13	1.67 ± 0.04	Sy1.5
29	165	NGC 3281	415 ± 9	1509 ± 29	670 ± 5	2138 ± 15	1.78 ± 0.03	Sy2/CT
30	167	LEDA 093974	96 ± 23	256 ± 68	88 ± 1	242 ± 2	1.56 ± 0.04	Sy2
31	171	NGC 3516	262 ± 20	651 ± 16	313 ± 2	778 ± 7	1.41 ± 0.04	Sy1.5
32	179	NGC 3783	502 ± 10	1530 ± 41	670 ± 5	2038 ± 11	1.66 ± 0.03	Sy1
33	185	NGC 3998	98 ± 22	133 ± 20	93 ± 1	151 ± 2	0.75 ± 0.05	LINER[a]
34	187	LEDA 38038	166 ± 8	614 ± 41	260 ± 1	803 ± 4	1.74 ± 0.03	Sy2
35	188	NGC 4051	346 ± 30	885 ± 42	472 ± 4	1153 ± 10	1.38 ± 0.04	Sy1.5
36	196	Mrk 766	220 ± 13	859 ± 20	317 ± 2	1177 ± 11	2.02 ± 0.04	Sy1.5
37	204	3C 273	276 ± 3	454 ± 7	277 ± 2	556 ± 6	1.92 ± 0.06	Blazar/FSRQ
38	206	NGC 4507	510 ± 4	1163 ± 31	550 ± 4	1476 ± 10	1.22 ± 0.02	Sy2
39	222	ESO 323-077	472 ± 3	902 ± 17	523 ± 4	1130 ± 8	0.96 ± 0.02	Sy1.2
40	225	MCG -03-34-064	453 ± 11	1873 ± 45	761 ± 5	2297 ± 16	1.72 ± 0.03	Sy1.8
41	228	MCG -06-30-015	280 ± 32	591 ± 11	334 ± 3	749 ± 7	1.24 ± 0.04	Sy1.2
42	230	4U 1344-60	207 ± 9	556 ± 28	267 ± 2	684 ± 6	1.44 ± 0.04	Sy1.5
43	231	IC 4329A	769 ± 12	1790 ± 34	998 ± 6	2093 ± 16	1.12 ± 0.03	Sy1.2
44	233	Mrk 279	141 ± 9	387 ± 28	143 ± 1	378 ± 3	1.49 ± 0.04	Sy1.5
45	237	NGC 5548	157 ± 5	409 ± 40	189 ± 1	520 ± 4	1.53 ± 0.04	Sy1.5
46	239	SBS 1419+480	46 ± 6	189 ± 13	84 ± 1	238 ± 2	1.60 ± 0.04	Sy1.5
47	241	Mrk 817	188 ± 10	669 ± 27	274 ± 2	940 ± 8	1.89 ± 0.04	Sy1.5
48	246	WKK 4438	94 ± 15	266 ± 12	115 ± 1	325 ± 3	1.60 ± 0.04	Sy1
49	247	IC 4518A	243 ± 27	677 ± 22	240 ± 2	963 ± 8	2.14 ± 0.04	Sy2
50	248	Mrk 841	126 ± 13	372 ± 25	161 ± 1	445 ± 4	1.57 ± 0.04	Sy1

TABLE 1
Continued.

Serial NO. (1)	BAT No. (2)	Object name (3)	F_{S9W} (mJy) (4)	F_{L18W} (mJy) (5)	F_{W3} (mJy) (6)	F_{W4} (mJy) (7)	$\alpha \pm \delta\alpha$ (8)	Type (9)
51	264	NGC 5995	325 ± 19	671 ± 4	368 ± 3	856 ± 6	1.28 ± 0.04	Sy2
52	277	Mrk 1498	67 ± 12	214 ± 21	95 ± 1	272 ± 3	1.62 ± 0.04	Sy1.9
53	285	3C 345	102 ± 7	353 ± 8	30 ± 0.3	76 ± 1	1.06 ± 0.04	Blazar/FSRQ
54	317	NGC 6300	277 ± 24	1336 ± 97	475 ± 4	1793 ± 15	2.05 ± 0.04	Sy2
55	360	[HB89] 1821+643	131 ± 4	326 ± 10	164 ± 1	457 ± 4	1.54 ± 0.04	Sy1/RL
56	372	FAIRALL 0049	411 ± 20	920 ± 59	450 ± 4	1246 ± 10	1.40 ± 0.04	Sy2
57	374	ESO 103-035	300 ± 25	1446 ± 12	569 ± 4	2089 ± 17	2.01 ± 0.04	Sy2
58	377	3C 390.3	90 ± 10	242 ± 17	127 ± 1	263 ± 3	1.13 ± 0.04	Sy1/RL
59	378	Fairall 0051	301 ± 7	697 ± 62	350 ± 2	883 ± 7	1.37 ± 0.03	Sy1
60	401	ESO 141-G 055	150 ± 5	233 ± 38	164 ± 1	303 ± 3	0.91 ± 0.04	Sy1
61	404	2MASX J19301380+3410495	130 ± 12	254 ± 23	170 ± 1	352 ± 3	1.12 ± 0.04	Sy1
62	418	NGC 6860	155 ± 13	357 ± 61	251 ± 2	412 ± 4	0.78 ± 0.05	Sy1
63	425	4C +74.26	147 ± 6	175 ± 9	135 ± 1	173 ± 2	0.36 ± 0.05	Sy1/RL
64	427	Mrk 509	247 ± 18	499 ± 17	268 ± 2	642 ± 6	1.34 ± 0.04	Sy1.2
65	429	2MASX J21140128+8204483	71 ± 5	105 ± 32	70 ± 0.5	165 ± 2	1.31 ± 0.05	Sy1/RL
66	445	Mrk 520	146 ± 12	320 ± 11	164 ± 1	437 ± 4	1.51 ± 0.04	Sy1.9
67	447	BL Lac	247 ± 36	319 ± 34	363 ± 3	722 ± 6	0.87 ± 0.03	Blazar/BL Lac
68	451	3C 445	141 ± 13	358 ± 6	148 ± 1	267 ± 3	1.09 ± 0.05	Sy1.5/RL
69	456	NGC 7319	88 ± 14	158 ± 8	78 ± 1	201 ± 2	1.46 ± 0.04	Sy2
70	466	Mrk 926	60 ± 3	214 ± 36	122 ± 1	252 ± 3	1.15 ± 0.05	Sy1.5
71	468	NGC 7603	295 ± 11	321 ± 12	324 ± 2	381 ± 3	0.24 ± 0.04	Sy1.5

NOTE. — Col. 1: serial number. Col. 2: Object number in the 22-month *Swift*/BAT hard X-ray survey catalog (Tueller et al. 2010). Col. 3: Object name. Col. 4 and 5: The flux and error in S9W (9 μm) and L18W (18 μm) taken from the *AKARI*/PSC in units of mJy. Col. 6 and 7: The flux and error in W3 (12 μm) and W4 (22 μm) taken from the *WISE* All-sky Source Catalog in units of mJy. Col. 8: The slope and error of the SED of each source Col. 9: Optical AGN type taken from Tueller et al. (2010) or from other literature as listed below:

REFERENCES. — [a]Véron-Cetty & Véron (2010);

TABLE 2
NUMBER OF CROSS-IDENTIFIED AGN FOR EACH TYPE

		Source type					total
Sy1 (1)	Sy2 (2)	LINER (3)	BL (4)	RL1 (5)	RL2 (6)	CT (7)	(8)
38	18	1	4	7	2	1	71

NOTE. — Col. 1–7: Numbers of detected sources in 4-bands of *AKARI* and *WISE* for each AGN type. Col. 1: Seyfert 1 including Seyfert 1.2 and 1.5. Col. 2: Seyfert 2 including Seyfert 1.8 and 1.9. Col. 3: LINERs. Col. 4: Blazars. Col. 5: type 1 radio-loud AGN. Col. 6: type 2 radio-loud AGN. Col. 7: Compton-thick AGN. Col. 8: Total numbers of cross-identified sources, i.e., sum of columns 1 through 7.

3. ANALYSIS AND RESULTS

3.1. *Relative flux variations*

We use relative flux ratios between *AKARI* and *WISE* as a basic quantity to describe the time variation of the sources. However, we do not use them directly, but only after applying various corrections as detailed later. The relative flux ratio of the i-th source, R_r^i, is defined as:

$$R_r^i = \frac{F_W^i - F_A^i}{F_A^i}, \tag{2}$$

where F_W^i and F_A^i are fluxes of i-th source in *WISE* and *AKARI* catalogs, respectively. Because of the proximity of the central wavelengths, we compare fluxes of *WISE* 12 μm (W3) with *AKARI* 9 μm (S9W), and *WISE* 22 μm (W4) with *AKARI* 18 μm (L18W), respectively. Thus we obtain two sets of relative flux rations; one in S9W-W3 band and the other in L18W-W4 band. As the central wave lengths of the data, we use the isophotal wavelengths defined as 8.61, 11.56, 18.39, and 22.09 μm for S9W, W3, L18W, and W4, respectively (Ishihara et al. 2010; Wright et al. 2010). Because the observation bands of *AKARI* and *WISE* are slightly different, the difference must be corrected; the correction method will be explained in the next subsection §3.2.

3.2. *Correction of the band differences*

We calculate a correction factor due to the band difference for each source using the SED. We assume that the SED has a power-law form, which is a good approximation for AGN except for local emission/absorption structures. We use *AKARI* and *WISE* data themselves to determine the power-law slope of the SED. Of course, because the source may be time variable, *AKARI* and *WISE* data may show systematic offset. However, the power-law slope of SED is considered to be rather insensitive to the time variation. Because of the proximity of the corresponding *AKARI* and *WISE* bands, the slope is basically determined to connect the weighted average of W3 and S9W fluxes and that of W4 and L18W fluxes. In reality, the *WISE* data have much better statistics than the *AKARI* data. Thus the slope is mostly determined by the *WISE* data. We use the isophotal wavelengths described in the previous subsection as the center of the wave bands, and ignored their errors.

Once the slope is determined, we can calculate the correction factor, R_c^i, to the relative flux ratio as follows,

$$R_c^i = \left(\frac{\lambda_W}{\lambda_A}\right)^{\alpha^i} - 1, \tag{3}$$

where λ_W and λ_A are the isophotal wavelengths of *WISE* and *AKARI*, respectively. α^i is the slope of the SED of i-th source. In addition, the error of R_c^i, δR_c^i, is calculated as,

$$\delta R_c^i = \left(\frac{\lambda_W}{\lambda_A}\right)^{\alpha^i} \log\left(\frac{\lambda_W}{\lambda_A}\right) \times \delta\alpha^i, \tag{4}$$

where $\delta\alpha^i$ is the error of α^i. Average values of R_c^i were 0.49 and 0.29 in S9W-W3 and L18W-W4, respectively, for the whole samples, and those of errors were 7×10^{-3} and 4×10^{-3}, respectively.

We calculated $R_r^i - R_c^i$ for each source and evaluated their distribution. However, the center of the distribution in S9W-W3 bands calculated for the whole sample was -0.25, significantly offset from zero. Similar tendency was also seen in the L18W-W4 band with smaller magnitude (-0.04). Several reasons may be conceivable for the offsets: for example, shifts of the center of the wave bands from the isophotal values due to the different slope from Vega, and the local structures of the emission/absorption lines. We represent the offsets as r, and will subtract it from the relative flux ratios in the subsequent analysis.

3.3. *Variability criteria*

Using the relative flux ratios, we search the catalogs for variable sources. For this purpose, we normalize the ratios with the errors, because the normalized ratios are directly related to the significance of variations. Thus, we introduce variability criteria S following Enya et al. (2002c) as follows:

$$S^i = \frac{R_r^i - R_c^i - r}{\sqrt{\delta R_r^{i\,2} + \delta R_c^{i\,2}}}. \tag{5}$$

Here, R_r^i is the relative flux ratio defined in Equation (2), R_c^i and δR_c^i are the correction to the relative flux ratio due to the wave band difference and its error, respectively, r is an average of $R_r^i - R_c^i$ defined for the total samples or each subtype depending on the samples under consideration. δR_r^i is an error of R_r^i defined as:

$$\left(\frac{\delta R_r^i}{R_r^i}\right)^2 = \left(\frac{\delta F_W^i}{F_W^i}\right)^2 + \left(\frac{\delta F_A^i}{F_A^i}\right)^2 + \epsilon^2 \tag{6}$$

where F_W^i and F_A^i are *WISE* and *AKARI* fluxes, respectively, and δF_W^i and δF_A^i are their respective errors. We also introduced a constant factor, ϵ, to incorporate the cross-calibration error between *AKARI* and *WISE*. Cross-calibration analysis was done to evaluate ϵ, which is described in Appendix. ϵ is independent of types of the source, and is 1.5% and 4.1% for the S9W-W3 and L18W-W4, respectively. We note that the errors δR_r^i and δR_c^i are in reality not independent. This is because δR_c^i is determined by $\delta\alpha^i$, which originate from the errors of F_W^i and F_A^i. Thus the denominator of Equation (5) may be slightly overestimated. However, we adopted the definition of Equation (5) as this is conservative way to evaluate the significance of variability.

We show frequency distribution of S in a bar chart in Figure 1 for the S9W-W3 and L18W-W4 bands. It is clear that most of AGN have S concentrated around $S = 0$ with a few exceptions. These exceptional sources are strongly time variable ones. We list largely deviated sources with $> 8\sigma$ confidence limit, i.e., $|S| > 8$, in Table 3 (2 blazars and 1 RL1). The criterion of 8σ is selected rather arbitrarily, but is large enough to exclude any marginal sources. These are the best candidates of variable sources. Only 1 source, which is a blazar, shows significant variability in both bands.

After excluding significantly variable sources in Table 3, we calculated the standard deviation and error of S for the remaining samples. The standard deviation was 2.36 ± 0.20 and 1.17 ± 0.10 in the S9W-W3 and L18W-W4, respectively. Here, the errors represent 1σ confidence limit. It is immediately noticed that the standard deviation is significantly larger than unity for the S9W-W3 band. This means that the sample distribution in the S9W-W3 is much larger than

that expected from the pure statistical variations of the sources. On the other hand, the sample distribution in the L18W-W4 may be consistent to the pure statistical one. In order to evaluate the presence of extra scattering in the data, it is crucial to estimate the confidence interval of the standard deviations accurately. Calculation of the error of standard deviations assumes normal distribution of the data, which is not necessarily true in this case. Thus, we applied the bootstrap method to estimate the reliable confidence interval of the standard deviations. In the bootstrap method, no a priori assumption is made for the parent distribution of the data. The data themselves, S in this case, are assumed to compose the parent distribution, and samples are selected randomly allowing redundancy. This trial is repeated many times (2000 times in this case) to determine the confidence interval. The bootstrap method is applied for both S9W-W3 and L18W-W4 bands. We summarize all the results in Table 4. We could not calculate averages and standard deviations for CT AGN and LINER in both bands because the available sample is only one. Similarly, the results may not be reliable for RL2 and BL because of the small number of samples. The table also includes the errors of the standard deviations calculated assuming the normal distribution of the samples, i.e., standard deviation divided by $\sqrt{2(N-1)}$, where N is the number of samples. It is clear from the table that the standard deviation in the S9W-W3 band is significantly larger than unity for the whole category and for Seyfert 1s and 2s. This means that Seyferts as a whole may be more or less variable in the S9W-W3 band, although the time variations are difficult to detect individually. We evaluate the magnitude of time variations in the next subsection.
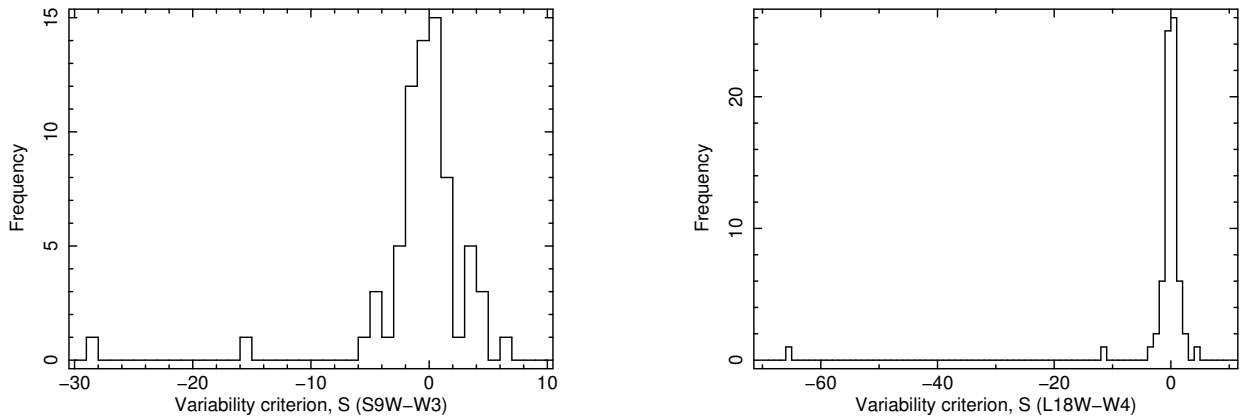

FIG. 1.— Distribution of the variability criteria, S defined in Equation 5. The abscissa shows S of each source, and the ordinate the number of sources. The left and right panels are histograms in the S9W-W3 and L18W-W4 bands, respectively. Total number of sources are both 71. In both histograms, the bin size is set to $\Delta S = 1$.

TABLE 3
SOURCES VARIABLE AT >8 SIGMA SIGNIFICANCE LEVEL

Object name	F_{S9W} (mJy)	F_{L18W} (mJy)	F_{W12} (mJy)	F_{W22} (mJy)	S S9W-W3 / L18W-W4	Type
(1)	(2)	(3)	(4)	(5)	(6)	(7)
3C 345	102 ± 7	353 ± 8	30.1 ± 0.3	76 ± 1	-28.8 / -66.0	Blazar
3C 273	276 ± 3	454 ± 7	277 ± 2	556 ± 6	-15.6 / -2.6	Blazar
3C 445	141 ± 13	358 ± 6	148 ± 1	267 ± 3	-0.9 / -11.3	type1 RL

NOTE. — Col. 1: Object name. Col. 2–3: Flux and error in the S9W and L18W bands taken from the *AKARI* catalog in units of mJy. Col. 4–5: Flux and error in the W3 and W4 bands taken from *WISE* all-sky source catalog in units of mJy, which are converted from that in units of magnitude by Equation 1. Col. 6: Variability criteria in the S9W-W3 and L18W-W4 bands estimated by Equation 5. Col. 7: Optical AGN type taken from Tueller et al. (2010); here RL means radio-loud AGN.

Type	N	S			
		average	standard deviation	confidence interval (95%)	
				normal dist.	boot strap
(1)	(2)	(3)	(4)	(5)	(6)
			S9W-W3 band		
All	69	0.00 ± 0.19	2.36	1.97–2.75	1.92–2.75
Sy1	38	-0.11 ± 0.12	2.33	1.80–2.86	1.63–2.89
Sy2	18	-0.15 ± 0.31	2.69	1.79–3.59	1.74–3.37
RL1	7	-0.10 ± 0.10	1.77	0.77–2.77	0.93–2.17
RL2	2	0.47 ± 0.20	1.69	–	–
CT	1	$\cdots$	$\cdots$	$\cdots$	$\cdots$
LI	1	$\cdots$	$\cdots$	$\cdots$	$\cdots$
BL	2	7.97 ± 0.16	7.30 ± 5.16	–	–
			L18W-W4 band		
All	69	0.01 ± 0.14	1.17	0.97–1.37	0.88–1.43
Sy1	38	-0.11 ± 0.14	1.00	0.76–1.24	0.66–1.32
Sy2	18	0.10 ± 0.11	1.14	0.77–1.51	0.74–1.41
RL1	6	0.25 ± 0.22	0.98	0.37–1.59	0.24–1.29
RL2	2	0.09 ± 0.07	1.51	–	–
CT	1	$\cdots$	$\cdots$	$\cdots$	$\cdots$
LI	1	$\cdots$	$\cdots$	$\cdots$	$\cdots$
BL	3	0.54 ± 0.17	3.47 ± 1.74	0.06–6.88	< 3.96

NOTE. — Col. 1: Object type. Col. 2: Number of sources in each subtype, from which significantly variable sources listed in Table 3 are excluded. Col. 3: Average and error of variability criteria, S. Col. 4: standard deviation of variability criteria, S. Col. 5: Confidence interval of the standard deviation in 95% confidence limit calculated assuming the normal distribution of the samples. Col.6: Same as column 5 but calculated using the boot strap method.

3.4. *Fractional variability in mid-IR band*

In order to quantify the time variations of the sample as a whole, we introduce the fractional variation defined as the flux variation normalized by the weighted-mean average flux. They are defined as:

$$D^i = \frac{F_W^i - (1 + R_c^i + r)F_A^i}{\overline{F^i}} \tag{7}$$

$$\overline{F^i} = \frac{\delta F_A^{i\,2} F_W^i + \delta F_W^{i\,2}(1 + R_c^i + r)F_A^i}{\delta F_A^{i\,2} + \delta F_W^{i\,2}} \tag{8}$$

Here, D^i is the fractional variation, in which the weighted-mean flux $\overline{F^i}$ is used to normalize it. In this analysis, we excluded significantly variable sources in Table 3.

We show frequency distribution of D^i in a bar chart in Figure 2 for the whole samples. The width of the distribution indicates the relative variability of the samples, but caution should be paid to the contribution of the statistical errors. The width results from both the statistical variations and the intrinsic time variations. The former is defined by the statistical errors of the data. The statistical variations of D^i, which is denoted as $\delta_s D^i$ hereafter, is estimated as follows:

$$(\delta_s D^i)^2 = \left\{ \left(\frac{\delta F_W^i}{\overline{F^i}}\right)^2 + \left(\frac{1 + R_c^i + r}{\overline{F^i}} \delta F_A^i\right)^2 \right\} \tag{9}$$

Here we ignore errors of R_c^i and $\overline{F^i}$, because they originate from the errors of F_W^i and F_A^i and do not compose of independent errors. Using this equation, we define, σ_D^{int}, the standard deviation corresponding to the intrinsic time variation of the sample as follows:

$$\sigma_D^{\mathrm{int}\,2} = \frac{1}{N-1} \sum_{i=1}^{n} \{(D^i - \bar{D})^2 - (\delta_s D^i)^2\}. \tag{10}$$

In this definition of σ_D^{int}, contribution from the statistical variation is subtracted. The results are summarized in Table 5, in which the confidence intervals of σ_D^{int} are calculated with two methods, one assuming the normal distribution of the samples and the other using the boot strap method. We found that Seyfert 1 in the S9W-W3 band show significant variability of 13% (6–18%) in 95% confidence limit. Seyfert 2 and RL1 AGN show a hint of variability, but the significance is low.
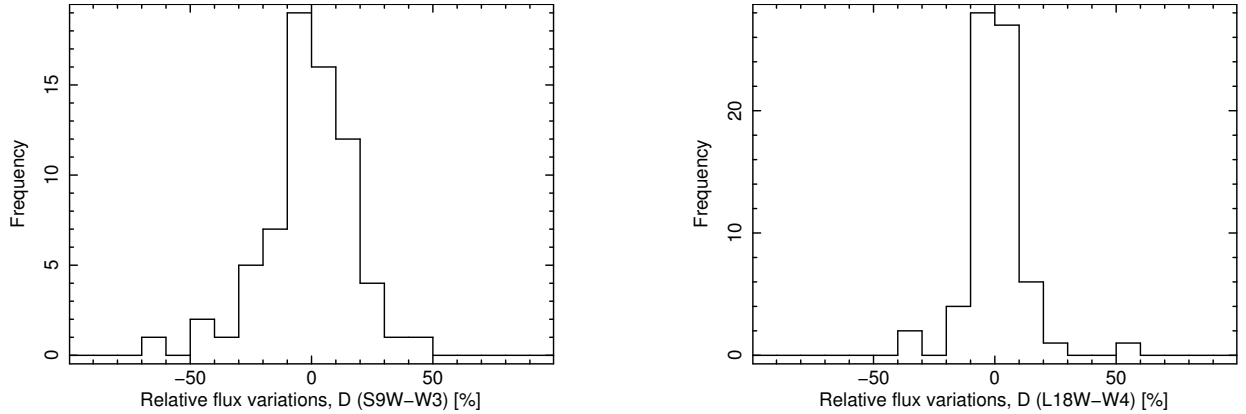
Fɪɢ. 2.— Frequency distribution of the relative flux variations for the total sample of AGN in the S9W-W3 band (left panel) and L18W-W4 band (right panel). The abscissa shows relative flux variations, D^i, in units of %. The ordinate shows the number of sources.

TABLE 5
Sᴛᴀɴᴅᴀʀᴅ ᴅᴇᴠɪᴀᴛɪᴏɴs ᴏF ᴛʜᴇ Fʀᴀᴄᴛɪᴏɴᴀʟ ᴠᴀʀɪᴀʙɪʟɪᴛʏ ᴅᴜᴇ ᴛᴏ ᴛʜᴇ ɪɴᴛʀɪɴsɪᴄ ᴛɪᴍᴇ ᴠᴀʀɪᴀᴛɪᴏɴs, σ_D^{int}, ᴀɴᴅ ᴛʜᴇɪʀ ᴄᴏɴFɪᴅᴇɴᴄᴇ ɪɴᴛᴇʀᴠᴀʟs

Type	N	variability fraction		
		standard deviation	confidence interval (95%)	
		%	normal dist.	boot strap
(1)	(2)	(3)	(4)	(5)
S9W-W3 bands				
All	69	14.4	11.3–17.5	7.9–19.5
Sy1	38	13.2	9.5–16.9	6.2–18.0
Sy2	18	19.5	10.9–28.1	< 28.4
RL1	7	11.5	3.2–19.8	< 16.5
RL2	2	< 14.4	–	–
CT	1	⋯	⋯	⋯
LI	1	⋯	⋯	⋯
BL	2	< 3.1	—	—
L18W-W4 bands				
All	69	5.2	3.2–7.2	< 19.5
Sy1	38	< 1.0	< 1.8	< 6.1
Sy2	18	4.2	0.5–7.9	< 12.3
RL1	6	< 3.8	< 2.1	< 7.0
RL2	2	6.7	< 18.5	–
CT	1	⋯	⋯	⋯
LI	1	⋯	⋯	⋯
BL	3	32.7	< 65.6	< 35.6

Nᴏᴛᴇ. — Col. 1: Object type. Col. 2: Number of sources in each subsample, from which the variable sources in Table 3 are excluded. Col. 3: standard deviation of fractional variability. Col. 4: Confidence interval of the standard deviation in 95% confidence limit calculated assuming the normal distribution of the samples. Col.5: Same as column 4 but calculated using the boot strap method.

4. DISCUSSION

We studied time variability of AGN in mid-IR bands combining the all-sky survey catalogs of *AKARI* and *WISE*. We found 3 significantly variable sources (2 blazars and 1 RL1) in addition to the variability of Sy1 as a whole reaching 6–18% in a relative amplitude in the S9W-W3 band. We discuss possible systematics in the calculation first, then the implication of the results for the individual sources and for Sy1 as a whole.

4.1. Other systematics

Although we have accounted for many systematic effects in comparing the *AKARI* and *WISE* catalogs, there may be some other small effects remaining, e.g., differences of the PSFs, or read out noise. The aperture radius of *AKARI* is 7″.5 in S9W and L18W. On the other hand, we used results of the profile-fit photometry by *WISE* whose FWHM is 6″.5 and 12″.0 in W3 and W4, respectively. In order to evaluate systematics due to the difference of the PSFs between *AKARI* and *WISE* (i.e., aperture and profile-fit photometry), we calculated flux ratios between the aperture

and the profile-fitt photometry of *WISE*. We used aperture magnitudes measured for $8''.25$ and $11''.0$ in radius in W3 and W4, respectively, which are the closest radii to those of *AKARI*. The average flux ratios of profile-fit-to-aperture photometry were 1.00 and 1.44 in W3 and W4, respectively. Note that offsets of the flux ratios from 1.0 is not important because they were subtracted as r in the course of the calculation. The standard deviation of the average flux ratio was 0.002 and 0.034 in W3 and W4, respectively. The small value of the standard deviation means that the effect of the difference of photometry is negligible than variability.

4.2. *Variable sources in mid-IR band*

4.2.1. *Blazars*

Among the 3 variable sources, two are 3C 345 and 3C 273, famous blazars/FSRQs. 3C 345 was highly variable in both S9W-W3 and L18W-W4 bands, and its fractional variation reached $\sim300\%$ and 400% in the respective band. On the other hand, 3C 273 was variable only in S9W-W3 band with a fractional variation of $\sim50\%$.

3C 345 is observationally known to be highly variable in all wave bands including mid-IR. Although observations were rather sparse in mid-IR, time variations of an order of magnitude was clearly detected. Time variations of 60–70% in a few years were observed in the monitoring at Palomar Observatory at 1.2–10.2 μm (Bregman et al. 1986). They generally had corresponding events in the optical band. Similar amplitude of variations ($\sim50\%$ in 12–25 μm) in a few months were observed by pointed *IRAS* observations (Edelson & Malkan 1987). The monitoring campaign from radio through optical bands in 2005-2006 showed the evolution of SEDs with mid-IR variations reaching $\sim100\%$ in a few years (Bach et al. 2007). Large time variations we detected in the mid-IR bands, a factor of ~3–4 in 4 years, may be regarded as one of the typical behaviors of 3C 345.

3C 273 is a famous, bright, and nearby blazar and is well studied at all wavelengths (Courvoisier 1998). Monitoring observations over two decades at 10.6 μm, revealed time variations of ~1 mag in a few years (Neugebauer & Matthews 1999). The monitoring campaign from radio through optical bands in 2005-2006 showed the evolution of SEDs which may correspond to mid-IR variations of $\sim50\%$ in a few years (Bach et al. 2007). Characteristics of blazar in 3C 273 may be more clearly recognized at near-IR than at optical wavelengths. Monitoring observations for 4 years in the near-IR and radio bands detected several flares, in which the near-IR fluxes increased by a factor of a few (Robson et al. 1993). McHardy et al. (1999) showed that the X-ray (3-20 keV) and near-IR (K band, 2.2 μm) variations of 3C 273 were highly correlated. The strong correlation supports the synchrotron self-Compton model, where the seed photons of near-IR band are synchrotron photons from the jets. Compared to these past observations, significant variations we detected from 3C 273 in the S9W-W3 band ($\sim50\%$ in 4 years) may be typical of this source.

Both blazars are monitored frequently in R-band with two nearly identical photometers-polarimeters of AZT-8 (the Crimean Observatory, Ukraine) and LX-200 (St. Petersburg University, Russia) since 2005 or 2006. The light curves of 3C 345 and 3C 273 both show flaring events superposed on the gradual variations. Because the light curves cover the *AKARI* and *WISE* survey periods, we can roughly infer the R-band variations between these two surveys: ~1 mag decrease for 3C 345 and ~0.2 mag decrease for 3C 273. Although direct comparison is difficult due to the wavelength difference, the decreasing trend in the R-band is consistent to our mid-IR results (S<0).

4.2.2. *Radio-loud AGN*

3C 445 is a nearby ($z = 0.056$) FR II radio galaxy (Hewitt & Burbidge 1991; Kronberg et al. 1986). We detected a flux decrease of $\sim50\%$ in L18W-W4 band whereas the decrease was insignificant at $\sim9\%$ in S9W-W3 band. Similar variation in mid-IR emission from 3C 445 is not reported so far.

Origin of the mid-IR emission from radio-loud AGN is not well understood yet. From the comparison of SEDs between BLRGs and a blazar (3C 273), Grandi & Palumbo (2007) suggested that although the jet contribution in X-ray band does not exceed 45%, the SEDs of powerful BLRGs likely hide a jet with a spectral shape very similar to that of 3C 273, and the IR bump of radio galaxies recalls the synchrotron peak of blazars. On the other hand, from the statistical analysis of 19 3CRR radio-loud galaxies including 3C 445 in mid- to far-IR observations, Dicken et al. (2010) concluded that the dominant heating mechanism for mid-IR emitting dust is AGN illumination based on the correlation between mid-IR luminosities and the AGN power indicator [OIII].

If we invoke only the AGN illumination, the large fractional variation ($\sim50\%$) detected from 3C 445 may be difficult to explain. According to the clumpy torus variability model of type 1 AGN (Hönig & Kishimoto 2011), variation in L18W-W4 bands is predicted to be much smaller than that detected from 3C 445, even if a very strong AGN flare with 50% total luminosity were to be occur. The large variability observed from 3C 445 may instead be interpreted as the contribution of the non-thermal emission from the jet.

4.3 *Fractional variability for each type of AGN*

Through the analysis of fractional variability in Section 3.4, we found that Sy1 show variability $\sim13\%$ (6-18%) in S9W-W3 bands at the 95% confidence limit. Heretofore, few data exist on 10 μm variability on long timescales for Seyferts. In a two decade long multiwavelength monitoring campaign, Neugebauer & Matthews (1999) found a mean variability of $\sim10\%$ at 10 μm from 25 radio-quiet quasars. Our result indicates for the first time that Sy1 may have intrinsically similar variability as quasars in the mid-IR band.

We could not detect significant variations from other subsamples mostly due to the limited statistics. However, this

does not exclude the presence of similar variability as Sy1 for other types of AGN. This is true especially for Sy2, whose upper limit of fractional variations in S9W-W3 band was 28%. Thus our results allow presence of similar time variations in Sy1 and Sy2.

4.4 *Variability time scale of torus emission*

Because the IR emission from Sy is considered to originate from the dusty torus illuminated by AGN, we first try to interpret the variability we detected from Sy1 as that of the torus emission. The thermal equilibrium relation of graphite grains may be used to give the dust location as a function of its temperature as,

$$r = \frac{1.3}{3} \left(\frac{L_{\mathrm{UV}}}{10^{46} \mathrm{\ erg\ s^{-1}}} \right)^{1/2} \left(\frac{T}{1500 \mathrm{\ K}} \right)^{-2.8} \mathrm{pc}, \tag{11}$$

where r is the distance from the central region, L_{UV} is the UV luminosity, T is the grain temperature (Barvainis 1987). We included in this equation a factor of $\sim 1/3$ (Kishimoto et al. 2007; Nenkova et al. 2008; Kawaguchi & Mori 2010) as indicated by the time lag measurements of four nearby Sy1 galaxies by Suganuma et al. (2006).

If we assume a central X-ray luminosity of $10^{44} \mathrm{\ erg\ s^{-1}}$, which is a median value of our sample of AGN, the luminosity in UV band may be estimated as $\sim (2\text{–}3) \times 10^{45} \mathrm{\ erg\ s^{-1}}$ (Elvis et al. 1994; Vasudevan & Fabian 2007). Using this UV luminosity, dust grains at 300 K, whose emission peaks at 9 μm, are estimated to lie 10 pc ($\sim$30 light-year) from the central region. If we interpret this distance naively, it seems to be too large compared to the rapid time variations we detected ($\sim$13% in 4-years). However, a detailed model is required to make quantitative evaluation whether the distance is indeed incompatible with our result of time variations. Such detailed modeling is out of the scope of the present paper, but we show an example of the model from the literature in the next subsection and discuss a possible constraint on the dust distribution.

4.5 *Dust distribution in the torus*

According to the variability model of type 1 AGN (Hönig & Kishimoto 2010, 2011), time variation in the mid-IR band as a response to the variation of the incident radiation on the torus is largely dependent on dust distribution in the torus. Hönig & Kishimoto (2011) defined dust distribution in the torus with the surface filling factor which has a radial dependence of r^α. When dust distribution is flat ($\alpha > -0.5$), their simulation shows no clear peak in the mid-IR band (8.5 μm in their simulation) as a response to the step function change of the incident AGN radiation. On the other hand, if dust distribution is narrow ($\alpha < -1.5$), i.e., its distribution is limited in terms of the distance from the AGN, the mid-IR emission shows delayed peak in the light curve. The time scale of mid-IR variations near the peak can be shorter than the light crossing time of the torus. In this case, the mid-IR emission is dominated by the Rayleigh-Jeans tail of the hot dust emission located in the inner torus, not by the peak blackbody emission of cooler dust. Although this is rather simplified view of time variations, if the mid-IR variability can be explained by the torus emission only, those detected in Sy1 ($\sim$13% in 4 years) prefer rather narrow distribution of dust in the torus. The mid-IR variability will become a useful tool to constrain dust distribution in AGN tori.

4.6 *Other origins of variability*

The variability we detected from Sy1 may have different origin than the torus. Here we consider the possibility of jet contribution. Most of Seyfert 1 show some degree of radio-loudness, which is inferred from the nuclear radio-to-optical luminosity ratios (Ho & Peng 2001). Also, elongated jet-like features were discovered from 14 Seyferts by the Very Large Array (VLA) surveys (Ho & Ulvestad 2001). Recently ejected jet may contribute to mid-IR variability. If this is the case, the jet activity should be observed with recent and future all-sky surveys in the radio band such as the LOw Frequency ARray (LOFAR) and the square Kilometer Array (SKA).

5. CONCLUSIONS

We studied mid-IR variability of AGN systematically in order to constrain the geometry of the dusty torus. Combining two sets of all-sky survey data from *AKARI* and *WISE*, we calculated time variations of each source excluding the systematic effects as much as possible. As a result, we found 3 sources, 2 blazars and 1 RL1, significantly variable in the mid-IR band. We also estimated average variability for each type of AGN excluding the three variable sources. We found that Sy1 show significant variability of $\sim$13% (6–18% in the 95% confidence interval) in the S9W-W3 band. Comparing the detected variation (13% in 4 years) with the model calculation for the type 1 AGN, we conjectured that, if the variation results from the torus, dust distribution in the torus should be narrow. Alternatively, it is also possible that the variation originates from the jets in Sy1, whose presence is suggested from the radio observations.

REFERENCES

Bach, U., Raiteri, C. M., Villata, M., et al. 2007, A&A, 464, 175
Barvainis, R. 1987, ApJ, 320, 537
Bregman, J. N., Glassgold, A. E., Huggins, P. J., et al. 1986, ApJ, 301, 708
Clavel, J., Wamsteker, W., & Glass, I. S. 1989, ApJ, 337, 236
Courvoisier, T. J.-L. 1998, A&A Rev., 9, 1
Dicken, D., Tadhunter, C., Axon, D., et al. 2010, ApJ, 722, 1333
Edelson, R. A., & Malkan, M. A. 1987, ApJ, 323, 516
Elvis, M., Wilkes, B. J., McDowell, J. C., et al. 1994, ApJS, 95, 1
Enya, K., Yoshii, Y., Kobayashi, Y., et al. 2002, ApJS, 141, 23
Enya, K., Yoshii, Y., Kobayashi, Y., et al. 2002, ApJS, 141, 31
Enya, K., Yoshii, Y., Kobayashi, Y., et al. 2002, ApJS, 141, 45
Gorjian, V., Werner, M. W., Jarrett, T. H., Cole, D. M., & Ressler, M. E. 2004, ApJ, 605, 156
Grandi, P., & Palumbo, G. G. C. 2007, ApJ, 659, 235
Hönig, S. F., & Kishimoto, M. 2010, A&A, 523, A27
Hönig, S. F., & Kishimoto, M. 2011, A&A, 534, A121
Haardt, F., & Maraschi, L. 1993, ApJ, 413, 507
Hewitt, A., & Burbidge, G. 1991, ApJS, 75, 297
Ho, L. C., & Peng, C. Y. 2001, ApJ, 555, 650
Ho, L. C., & Ulvestad, J. S. 2001, ApJS, 133, 77
Hoffman, D. I., Cutri, R. M., Masci, F. J., et al. 2012, AJ, 143, 118
Hunt, L. K., Zhekov, S., Salvati, M., Mannucci, F., & Stanga, R. M. 1994, A&A, 292, 67
Ishihara, D., et al. 2010, A&A, 514, A1
Jarrett, T. H., Cohen, M., Masci, F., et al. 2011, ApJ, 735, 112
Kawaguchi, T., & Mori, M. 2010, ApJ, 724, L183
Kishimoto, M., Hönig, S. F., Beckert, T., & Weigelt, G. 2007, A&A, 476, 713
Kozłowski, S., Kochanek, C. S., Stern, D., et al. 2010, ApJ, 716, 530
Kronberg, P. P., Wielebinski, R., & Graham, D. A. 1986, A&A, 169, 63
Matsuta, K., Gandhi, P., Dotani, T., et al. 2012, ApJ, 753, 104
McHardy, I., Lawson, A., Newsam, A., et al. 1999, MNRAS, 310, 571
Murakami, H., Baba, H., Barthel, P., et al. 2007, PASJ, 59, 369
Nenkova, M., Sirocky, M. M., Nikutta, R., Ivezić, Ž., & Elitzur, M. 2008, ApJ, 685, 160
Neugebauer, G., Soifer, B. T., Matthews, K., & Elias, J. H. 1989, AJ, 97, 957
Neugebauer, G., & Matthews, K. 1999, AJ, 118, 35
Robson, E. I., Litchfield, S. J., Gear, W. K., et al. 1993, MNRAS, 262, 249
Suganuma, M., Yoshii, Y., Kobayashi, Y., et al. 2006, ApJ, 639, 46
Tueller, J., et al. 2010, ApJS, 186, 378
Ulrich, M.-H., Maraschi, L., & Urry, C. M. 1997, ARA&A, 35, 445
Véron-Cetty, M.-P., & Véron, P. 2010, A&A, 518, A10
Vasudevan, R. V., & Fabian, A. C. 2007, MNRAS, 381, 1235
Wright, E. L., Eisenhardt, P. R. M., Mainzer, A. K., et al. 2010, AJ, 140, 1868
Yamamura, I., Makiuti, S., Ikeda, N., Fukuda, Y., Oyabu, S., Koga, T., & White, G. J. 2010, VizieR Online Data Catalogue, 2298, 0

APPENDIX

RELATIVE CALIBRATION ERRORS BETWEEN *AKARI* AND *WISE*

When comparing observed fluxes between different satellites, it is important to consider the relative calibration error accurately because the cataloged fluxes usually include various systematic effects. Therefore, we estimate relative calibration error between *AKARI* and *WISE* using bright stars commonly detected with these two satellites. We selected A- and F-type stars for this purpose (115/145 and 150/178 sources in S9W-W3/L18-W4) because their spectra in IR bands are rather featureless and are well approximated by a blackbody. As we need to use only bright stars to minimize the statistical errors, we plot the Signal-to-Noise ratio (S/N) of *AKARI* for A- and F-type stars commonly detected by *AKARI* and *WISE* in Figure 3. We select bright stars based on the following criteria on the *AKARI* fluxes:

- Flux > 800 mJy, and S/N > 50 in the *AKARI* S9W band; this leaves 38/57 sources for A-/F- type,

- Flux > 300 mJy, and S/N > 10 in the *AKARI* L18W band; this leaves 40/34 sources for A-/F- type.

Here, S/N is defined as the flux divided by its error.

We calculate relative flux ratio R_r defined in Equation 2 for the selected bright stars, and show the distributions in Figure 4. We then determined the center of the distribution by fitting a Gaussian; the results are summarized in Table 6. The non-zero values of R_r are mostly due to the band difference between *AKARI* and *WISE*. Thus we calculate the relative flux ratio R_r' due to the band difference for pure blackbody emission. If we assume temperature of F0 star (7200 K), R_r' is calculated as -0.428 and -0.301 in S9W-W3 and L18W-W4, respectively. Note that these values are rather insensitive to the selection of temperature, because the observation bands lie in the Rayleigh-Jeans region. The differences $R_r - R_r'$ between the observed and calculated values represent the calibration errors, and were –0.015 and –0.041. Therefore, we estimate the relative calibration error, $|(R_r' - R_r)/R_r'|$ between *AKARI* and *WISE* as 1.5% and 4.1% in S9W-W3 and L18W-W4, respectively.
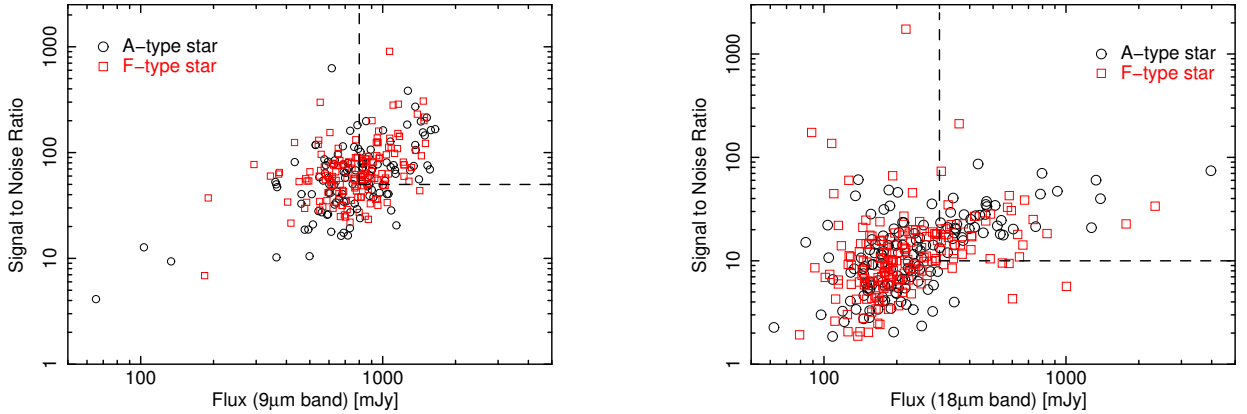

FIG. 3.— Signal-to-Noise (S/N) ratio, defined as the *AKARI* flux divided by its error, of A- and F-type stars detected by both *AKARI* and *WISE* are plotted against the *AKARI* fluxes. Left panel is for the S9W band and right panel for the L18W band. Black circles indicate A-type stars and red squares F-type stars. Bright stars with good S/N ratio, located in the upper-right region as indicated by the broken lines, are used for the estimation of the relative calibration error.

TABLE 6
SUMMARY OF R_r CALCULATION

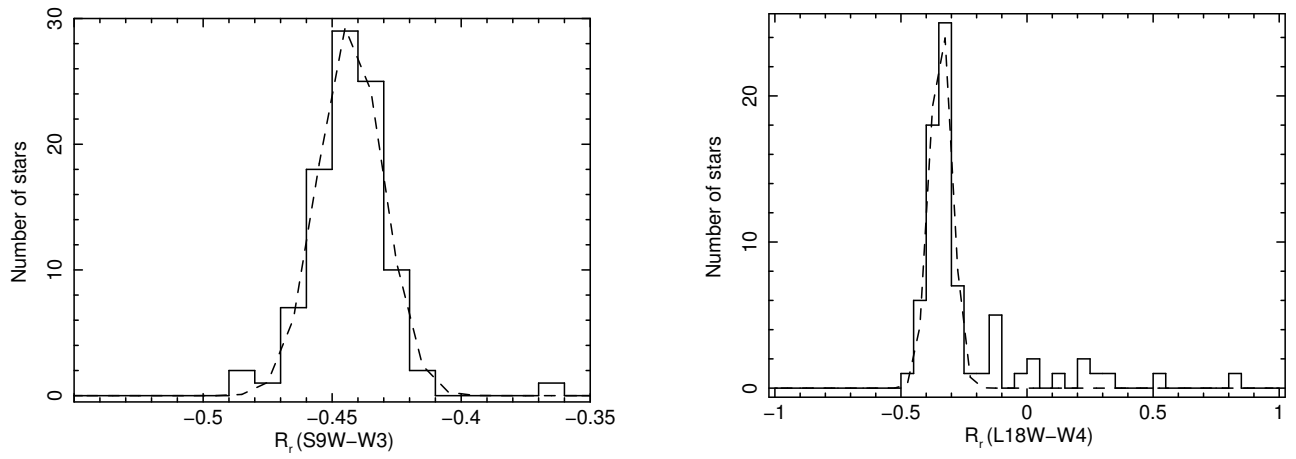| Wave band	Number of stars	Relative flux ratio		
AKARI-WISE	A/F type	R_r	R_r'	$R_r' - R_r$
S9W-W3	38/57	-0.443	-0.428	-0.015
L18W-W4	40/34	-0.342	-0.301	-0.041

FIG. 4.— Distribution of the relative flux ratio R_r between *AKARI* and *WISE* for the sum of A- and F-type stars. Left panel shows the distribution for S9W-W3 band, and right panel for L18W-W4 band. Broken line shows the best-fit Gaussian model, which is used to determine the center of the distribution.

JAXA Research and Development Report   JAXA-RR-16-010E

MID-INFRARED VARIABILITY OF ACTIVE GALACTIC NUCLEI WITH THE *AKARI* AND *WISE* ALL-SKY SURVEYS